Condition Monitoring of 154 kV HTS Cable Systems via Temporal Sliding LSTM Networks

GEON SEOK LEE[1], (Member, IEEE), **SU SIK BANG**[1], (Graduate Student Member, IEEE),
HOMER ALAN MANTOOTH[2], (Fellow, IEEE),
AND YONG-JUNE SHIN[1], (Senior Member, IEEE)
[1]School of Electrical and Electronic Engineering, Yonsei University, Seoul 03722, South Korea
[2]Department of Electrical Engineering, University of Arkansas, Fayetteville, AR 72701 USA

Corresponding author: Yong-June Shin (yongjune@yonsei.ac.kr)

ABSTRACT High-temperature superconducting (HTS) cables are expected to be installed in cable tunnels that are already constructed in urban districts. Therefore, the installation of normal joint boxes is inevitable, and it is necessary to develop a diagnostic methodology that considers both the existence of the joints and the electrical characteristics of HTS cables. In this work, temporal sliding long short-term memory (TS-LSTM) is proposed to estimate the locations of the joints that can be hidden by multiple reflections. TS-LSTM includes short-term TS-LSTM and long-term TS-LSTM for analyzing various time dependencies. The reflected signals of the actual joints, which are distinguished from multiple reflections, are analyzed via the chirplet transform (CT) which is one of the time-frequency (TF) analysis methods. The proposed condition monitoring method is applied to an AC 154 kV 600 MVA HTS cable system (1 km) connected to a real power grid network in Jeju, South Korea. For the validation of the proposed methodology, the dielectric and electrical characteristics of the 154 kV HTS cable system are monitored during the cooling process.

INDEX TERMS Condition monitoring, long short-term memory (LSTM), superconducting cable, temporal sliding LSTM (TS-LSTM) networks, time-frequency analysis.

I. INTRODUCTION

THE increasing use of electric vehicles and residential electricity usage accompanying the urbanization process have led to rapid increases in electricity demands. A high-temperature superconducting (HTS) cable can transmit large capacities even at low voltages; therefore, the use of HTS cables is desirable for reducing the size of new electric power facilities in urban areas where the underground infrastructure is already dense [1]. According to a study of the worldwide commercialization of HTS cables, two substations in Essen were connected by a 1 km-long 10 kV HTS cable as part of the Ampacity project in Germany [2], while in New York, a 600 m-long 138 kV HTS cable was successfully integrated with the Long Island Power Authority grid [3]. In Baiyin, China, an HTS power substation consisting of superconducting transformer, superconducting fault current limiter, superconducting magnetic energy storage system, and 10 kV

HTS cable was designed and demonstrated [4]. South Korea completed a demonstration test of a 1 km-long 154 kV HTS cable in Jeju and commenced commercial operation of a 1 km-long 23 kV HTS cable in 2019 [5].

The improvement of power quality and reliability is another major requirement for future urban energy planning and management [1]. A literature review of studies on the safe and stable operation of conventional power cables in recent years shows various condition monitoring and fault diagnosis techniques, such as partial discharge (PD), sheath testing, loss tangent, and reflectometry. For PD tests, in [6], a random-forest-based feature selection algorithm for the PD of high voltage (HV) cables was presented. Additionally, chaos synchronization–based characteristic extraction and clustering were recently used to improve the identification of defect types [7]. High-frequency-current transformer-based approaches include extraction of the HV cable transfer function [8], fault localization [9] and finite-difference time domain models of PD sensors [10]. In addition to the PD tests, as demonstrated in [11], a numerical model of cable

---

The associate editor coordinating the review of this manuscript and approving it for publication was Guangya Yang.

sheath current was revised, and the revised phasor-domain model was used to estimate the fault location. Even for cross-bonded cable systems that pose challenges for diagnostic method, fault detection methodologies via sheath currents have been developed [12], [13]. In addition, the methodologies for the monitoring of the effects of moisture and temperature on cable insulation have been developed based on loss tangent measurements [14], [15]. Lastly, based on the type of incident signals, reflectometry methodologies such as time domain reflectometry (TDR) [14], spread spectrum time domain reflectometry (SSTDR) [16], time-frequency domain reflectometry (TFDR) [17], and power line modems TFDR [18] have been applied to fault detection in power cables. Additionally, a diagnostic technique for underground DC cables using high-frequency noise patterns [19] and a Raman spectroscopic measurement technique for monitoring the degassing process of cross-linked polyethylene cables have been developed [20]. However, HTS cables are still in relative infancy compared to conventional cables, and condition monitoring techniques optimized for HTS cables have rarely been developed.

For more than 60 % of the urban areas of South Korea, the actual distance between any two adjacent substations is 1-3 km. Additionally, the installation of HTS cables between such adjacent substations along the existing power cable tunnels requires two or more joints [21]. Previous studies have not considered the presence of multiple joints. Owing to multiple reflections, distinguishing multiple joint boxes especially using reflectometry is a challenging problem. The multiple reflections imply that a signal is reflected repeatedly between the signal generator and the load. The current multiple reflection analysis includes the application of TDR to determine dielectric characteristics of both conductive and non-conductive systems. From a measured TDR trace, all the multiple reflections from the sensing probe section are considered [22], [23]. However, these conventional reflectometry methods aim to measure the complex dielectric permittivity of the entire material, not to analyze joint boxes individually. Thus, in this work, a condition monitoring methodology is proposed that takes into account both the electrical characteristics and installation conditions of HTS cables.

First, TFDR is used as a localization method for estimating the location of the cable termination and multiple joints to be monitored. To overcome the challenge of distinguishing and monitoring different joint boxes, time-frequency (TF) analysis and temporal sliding long short-term memory (TS-LSTM) networks are applied. The TF analysis includes the use of Wigner-Ville distribution (WVD) and chirplet transform (CT) which have been previously applied in high-resolution spectrum analysis [24]–[26]. In this study, WVD is used to measure the information contents of the reflected signals, and CT is used to monitor the reflected signals that depend on the conditions of the HTS cable systems. Together with WVD, a resolution enhancement method in the TF domain using TS-LSTM networks is proposed. TS-LSTM was first introduced in [27], [28] to improve the forget gates performance

of LSTM cells, and TS-LSTM enables the derivation of combinations of various signal attributes via time windowing.

The proposed condition monitoring method has been demonstrated for an AC 154 kV 600 MVA HTS cable system (1 km) connected to a real electric power grid in Jeju, South Korea. In the cooling process of the 154 kV HTS cable system from ambient temperature to 80 K, the results show that the TS-LSTM-based monitoring is more effective than that using conventional LSTM.

The remainder of this paper is organized as follows. Section II describes the theoretical background of TS-LSTM and the process of feature extraction. Section III describes the monitoring methods via TF analysis in detail. Section IV describes the method for training the data and experiments on the 154 kV HTS cable system. The performance of the proposed analysis method is also discussed based on experimental results. Finally, the results are discussed and conclusions are presented in Section V.

II. TEMPORAL SLIDING LONG SHORT-TERM MEMORY
A. FEATURE EXTRACTION

TS-LSTM networks were originally proposed for the modeling of temporal dynamics for skeleton-based action recognition [27], [28]. This method differs from the conventional skeleton-based action recognition in that the time series of human actions is partitioned and analyzed, and the features of the discriminative components are finally combined [27]–[30]. In particular, TS-LSTM can consider various temporal dependencies of action dynamics using different representations of the partition segment in short-term and long-term. In other words, TS-LSTM is useful for analyzing time series data with different time intervals or for analyzing signal information concentrated at specific time intervals.

Meanwhile, for reflectometry, an electrical signal transmitted through the tested cable depends on the characteristics of each section of the target cable, and the sectional characteristics are reflected in the corresponding time position of the electrical signal. Thus, it is also possible to apply TS-LSTM to cable monitoring results obtained using reflectometry measurements.

This section describes how the features of long-term and short-term TS-LSTMs are extracted to construct a TS-LSTM model. As shown in Fig. 1, an arbitrary signal, $s(t)$, which is transmitted and reflected on the cable can be rectangularly windowed over a chosen interval, W_L. Additionally, the windowed signal is partitioned by the number of sections, n, and converted to the TF domain by WVD calculating. The WVD of the transmitted signal is obtained as follows [31]:

$$WV_s(t, \omega) = \frac{1}{2\pi} \int s^*(t - \tau/2)s(t + \tau/2)e^{-j\omega\tau} d\tau. \quad (1)$$

Conventional monitoring techniques using WVD have analyzed reflected signals by assuming that multiple reflections do not exist [24], [32], [33]. However, if, for example, the location of the second joint and the multiple reflection
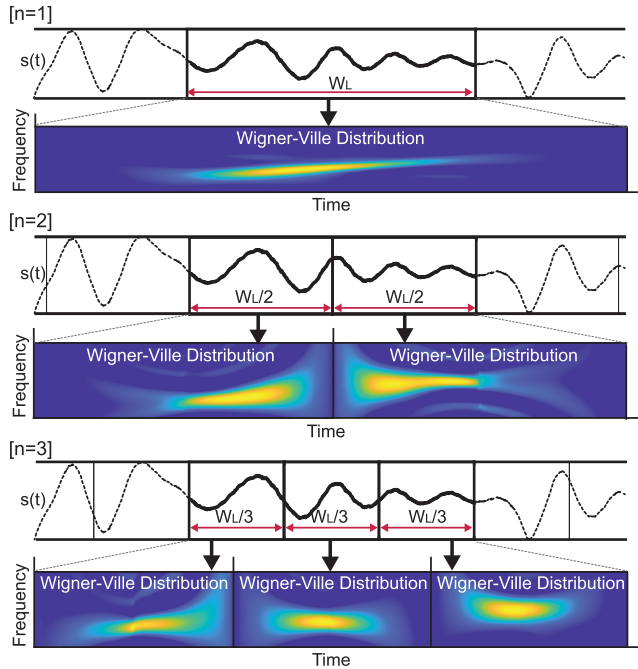
FIGURE 1. Feature extraction process.

location of the primary joint are similar, it is difficult to identify which of the joints is the target of the analysis. To resolve this ambiguity, TS-LSTM utilizes the quadratic nature of WVD to measure the information contents in the analyzed window. Owing to the non-linearity of the WVD, the WVD of multiple components produces cross-terms. As shown in Fig. 1, even for the same signal, the WVD of the windowed signal ($n = 1$) is distinct from the sum of the partitioned WVDs ($n = 2$ or 3) because the cross-terms in each section are generated differently. Thus, in the configuration of the long-term TS-LSTM, the WVDs of both the windowed signal ($n = 1$) and the signal reassembled after partition ($n = 2$ or 3) can be used as the input features.

Fig. 2 presents the input features of the short-term TS-LSTM with a length that is lesser than that of the long-term TS-LSTM. First, the WVD for each section can be expressed as a two-dimensional array as follows:

$$\hat{WV}_s(t) = [WV_s(t, 1), \cdots, WV_s(t, B)], \ \ t \in [t_1, t_1 + L] \quad (2)$$

where B is the length of the fast Fourier transform (FFT) and $L = W_L/n$ ($n = 2, 3, \cdots$) is the length of TS-LSTM module. The start point of the temporal stride is given by

$$t_1 = ST_L \cdot m, \quad m \in [0, (W_L/ST_L) - 1] \subset \mathbb{Z} \quad (3)$$

where ST_L is the temporal stride size. In this work, short-term TS-LSTM with temporal strides of size $ST_L = L$ and $L/2$ are used as two input features.

To summarize, the total model is obtained by integrating two long-term TS-LSTM modules and two short-term TS-LSTM modules. The integrated model uses different
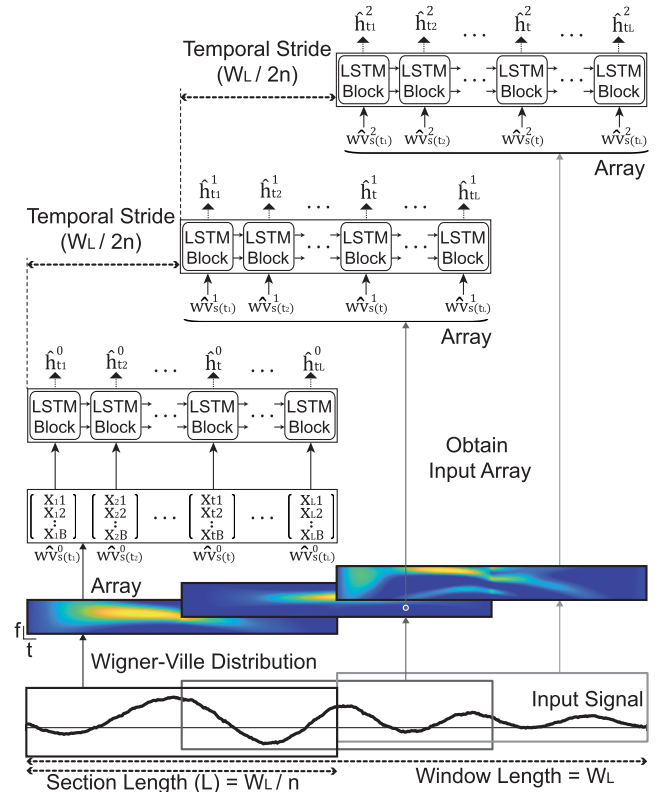

FIGURE 2. An illustration of the proposed short-term TS-LSTM module when $n = 2$ ($L = W_L/2$, and $ST_L = L/2$).

lengths of the segmented signals as inputs, so that the model can support the role of forget gates in the conventional LSTM.

B. NETWORK ARCHITECTURE

X_t^k is used to denote the input of the kth LSTM in a TS-LSTM module, as depicted in Fig. 2, and is related to the input features $X_t^k = \hat{WV}_s^k(t)$. Then, the equations of the LSTM cell are obtained as:

$$f_t^k = \sigma(W_{xf}^k X_t^k + W_{hf}^k h_{t-1}^k + W_{cf}^k c_{t-1}^k + b_f^k) \quad (4)$$

$$i_t^k = \sigma(W_{xi}^k X_t^k + W_{hi}^k h_{t-1}^k + W_{ci}^k c_{t-1}^k + b_i^k) \quad (5)$$

$$c_t^k = f_t^k c_{t-1}^k + i_t^k \tanh(W_{xc}^k X_t^k + W_{hc}^k h_{t-1}^k + b_c^k) \quad (6)$$

$$o_t^k = \sigma(W_{xo}^k X_t^k + W_{ho}^k h_{t-1}^k + W_{co}^k c_{t-1}^k + b_o^k) \quad (7)$$

$$h_t^k = o_t^k \tanh(c_t^k) \quad (8)$$

where sigmoid function σ and hyperbolic function tanh are non-linear activation functions, and f_t^k, i_t^k, and o_t^k are forget, input, and output gates vectors, respectively. h_t^k and c_t^k denote hidden state and internal cell state vectors, respectively. Also, W_{xj}^k, W_{hj}^k, W_{cj}^k, and b_j^k ($j = f, i, c, o$) are the weight matrices and bias vectors to be trained.

As shown in Fig. 3, the architectural arrangement consists of the TS-LSTM, sum-pooling, softmax activation, and classification layers. In the TS-LSTM layer, the number of LSTM cells, memory units, and activation functions are variable factors. The architecture of the proposed model varies with the change in the number of sections. Fig. 3 describes the
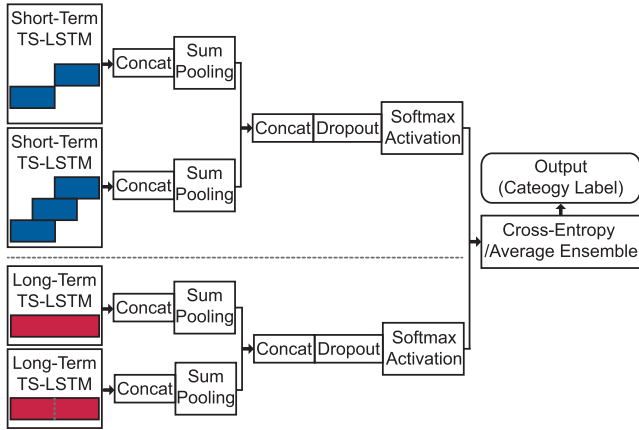
FIGURE 3. Overview of the proposed architecture of TS-LSTM model when *n* = 2.

details of the architecture when the number of sections is selected as $n = 2$. For two short-term TS-LSTM modules, temporal strides of L and $L/2$ are used as input features. For two long-term TS-LSTM modules, the WVD of the windowed signal ($n = 1$) and the sum of the partitioned WVDs ($n = 2$) are used as input features. After the TS-LSTM layer, the proposed model is constructed in the same structure. The value for hidden units in dropout layer is 0.4. In particular, in the classification layer, a cross-entropy cost function is used to train the TS-LSTM model, and average pooling is used to calculate and test the final output from softmax outputs [27], [28]. The variation in the performance difference of TS-LSTM with the number of sections, *n*, will be discussed in Section IV.

III. TIME-FREQUENCY ANALYSIS

To assess the efficacy of the proposed TS-LSTM, it is necessary to compare its performance to those of the previously used signal information measurement techniques. Therefore, this section introduces the conventional process of signal information measurement using TFDR and the Rényi entropy, respectively. Furthermore, new condition monitoring methods via CT are introduced, and the previously used method of anomaly malfunction detection in HTS cables for the performance evaluation comparison is also presented.

A. CONVENTIONAL Rényi ENTROPY

The generalized Rényi entropy is introduced as a tool that can quantify the concentration of energy. For performance comparison with TS-LSTM, the signal is converted into the TF domain via WVD in the same manner as for TS-LSTM, and the third-order Rényi entropy of (1) is written as:

$$H_3(WV_s) = -\frac{1}{2}\log_2 \iint WV_s(t,f)^3 dt df. \quad (9)$$

where WV_s is the normalized distribution [34], [35].

A small value of the third-order Rényi entropy implies that a large amount of signal information is concentrated. Therefore, the point used to separate the signal to be analyzed

and other signals that will not be used can be identified by comparing the size of the entropy values.

B. CONVENTIONAL TIME-FREQUENCY DOMAIN REFLECTOMETRY

TFDR can be used to calculate the amount of signal information as well as detect cable anomalies as follows: 1) TF cross-correlation (TFCC) is conventionally used in TFDR, particularly to resolve multiple elementary signals by measuring the signal information and indicating the separation points [32]. 2) The conventional methodologies for anomaly malfunction detection of HTS cables include the phase difference spectrum [24], [33] at the points where the reflected signals are measured using TFDR.

First, regarding the calculation of TFCC via TFDR, as the incident signal, a chirp signal with a Gaussian envelope is used and the incident signal is described by

$$s(t) = (\frac{\alpha}{\pi})^{1/4} e^{-\alpha(t-t_0)^2/2 + j\beta(t-t_0)^2/2 + j(\omega_0(t-t_0)+\varphi)} \quad (10)$$

where t_0, ω_0, and φ are time center, center frequency, and phase, respectively. α and β are signal design parameters [36]. WVD in (1) is used to convert the signal $s(t)$ in the time domain into a distribution in the TF domain. Let WV_s be the WVD of the incident signal and WV_r be the WVD of the reflected signal; then, the TFCC between the two signals is calculated as follows:

$$C_{sr}(t) = \frac{\int_{t'=t-T_s}^{t'=t+T_s} \int WV_r(t',\omega)WV_s(t'-t,\omega)d\omega dt'}{\int_{t'=t-T_s}^{t'=t+T_s} \int WV_r(t',\omega)d\omega dt' \cdot \iint WV_s(t,\omega)d\omega dt} \quad (11)$$

where T_s is the time duration of the incident signal [32]. The TFCC function quantifies the similarity between the incident and reflected signals as a value between 0 and 1, thereby indicating the presence of a reflected signal. Thus, the TFCC can also be used to measure the signal information that is similar to the incident signal.

Second, for the monitoring of the TF phase difference spectrum via TFDR, the equation that is obtained by substituting different signals s_1 and s_2 into s and s^* of (1) is called the cross-WVD, i.e. $WV_{s_1 s_2}$. Then, the TF phase difference spectrum is calculated as follows:

$$\theta_{s_1 s_2}(x,t,\omega) = tan^{-1}\left[\frac{Im\{WV_{s_1 s_2}(x,t,\omega)\}}{Re\{WV_{s_1 s_2}(x,t,\omega)\}}\right]$$
$$= x[k_{R2}(\omega) - k_{R1}(\omega)] \quad (12)$$

where k_R is the real part of the wave number and x is the location of the reflected signal [24]. Assuming that s_1 is the first measured reflected signal at the impedance change point, and s_2 is the signal measured in real-time at the same location, the TF phase difference spectrum can be used to monitor the variable wave number of the cable system. This is because the wave number varies depending on the electrical characteristics of the HTS cable system.

C. CHIRPLET TRANSFORM-BASED MONITORING INDEX

When two reflected signals are adjacent to each other, the reliability of the monitoring index derived from the WVD in (12) may be reduced owing to the cross-term. Thus, after the signal to be analyzed is distinguished from the multiple reflections via TS-LSTM, a new TF analysis method with a relatively low impact on cross-term generation is required. In this work, the new monitoring index is derived using the CT.

The CT can be interpreted as a type of short-time Fourier transform (STFT) because it uses a window to convert the signal to a TF distribution. The modulated window of the CT is a chirp signal with a Gaussian envelope which is a complex-valued function. Since the incident signal of the TFDR is also a chirp signal, the CT is expected to be able to window the reflected signals of the TFDR more precisely than a general Gaussian function. The window of the CT is given by:

$$g(t) = \frac{1}{(\sigma\sqrt{2\pi})^{1/2}} e^{-\frac{1}{2}[(t-t_c)/\sigma]^2 + j\omega_c(t-t_c)^2} \qquad (13)$$

where σ, ω_c, and t_c denote the spread of the signal, center frequency, and time center, respectively. Then, the CT is defined as:

$$CT_s(t, \omega) = \int s(t)g^*(t)e^{-\omega t}dt. \qquad (14)$$

with the complex window [25], [26]. Assuming that the parameter of (13) is set equal to the signal design parameter of the incident signal in (10), for the following relations $\sigma^2 = 2/\alpha$, $\omega_c = \omega_0$, and $t_c = t_0$, the CT is calculated as:

$$CT_s(t, \omega) = \frac{\alpha}{\pi} \cdot e^{-\frac{1}{4\alpha}(\omega-\omega_0)^2} \cdot e^{j(\omega t_0 + \varphi)} \qquad (15)$$

and the phase spectrum of (15) in the TF domain will therefore be given by

$$\Theta_s(t = t_0, \omega = \omega_0) = \omega_0 t_0 + \varphi. \qquad (16)$$

The phase spectrum in (16) is a variable function that depends on the temperature and pressure of a cable; therefore, it can be used as an index for monitoring the status of the HTS cable system.

IV. EXPERIMENTAL SETUP AND RESULTS

A. SOUTH KOREA 154 kV HTS CABLE SYSTEM (Jeju)

Fig. 4 shows the 154 kV 600 MVA HTS cable system that is used to validate both the TS-LSTM and the phase spectrum of the CT. In the three-phase 154 kV HTS cable system, each phase is approximately 1 km-long and has two normal joint (NJ) boxes. Meanwhile, liquid nitrogen flows from the A-phase, located in the Gumak conversion station (C/S), through the B-phase, to the C-phase in the HanLim C/S, for a total distance of 3 km. Two sets of 4 kW Stirling Cryocoolers are connected as the refrigeration system to cool the liquid nitrogen to 80 K.

In the monitoring of the 154 kV HTS cable system, the incident signal of the TFDR is applied from the A-phase termination installed at the Gumak C/S. The incident signal
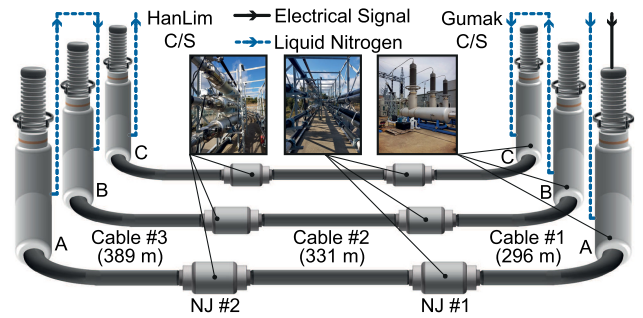
FIGURE 4. The configuration of the 154 kV HTS cable system.

is designed to have a bandwidth of 1 MHz, center frequency of 1.9 MHz, and time duration of 1950 ns. Since the three-phase HTS cables are not electrically connected to each other, the condition of the HTS cable system in the cooling process is monitored only for the A-phase in this work.

B. CONVENTIONAL TIME-FREQUENCY ANALYSIS RESULTS

The measurement of TDR is conducted to compare with the results of TFDR. Fig. 5(a) shows the data sample of TDR which normally uses a step pulse as an incident signal. As shown in Fig. 5(a), it is a challenging task to localize the position of NJ #1 and NJ #2 under the presence of noise without prior information on the 154 kV HTS cable system. Therefore, the use of a new incident signal and additional signal processing are required to distinguish the reflected signals from two NJs and to analyze the dielectric characteristics of the HTS cable system depending on temperature and pressure.

Fig. 5(b) shows the data sample of the TFDR in time domain when the incident signal is applied to the A-phase. The transmitted signal is reflected sequentially in the following positions: NJ #1 (296 m), a multiple reflection of NJ #1 (592 m) and NJ #2 (627 m), and termination (1016 m). As shown in the enlarged graph for the 500-850 m region in Fig. 5(b), the voltage of the incident signal is reduced by attenuation, and the multiple reflection of NJ #1 and reflected signal of NJ #2 overlap. Fig. 5(c) presents the WVD of the incident and reflected signals in the TF domain. Even in the TF domain, the multiple reflection of NJ #1 and reflected signal of NJ #2 including the cross-term are not distinguished from each other.

Figs. 5(d) and 5(e) show the results for the TFCC and the Rényi Entropy introduced in Section III, respectively. An examination of the results shown in Fig. 5(d) by calculating TFCC according to (11) shows that the position of NJ #1 is detected with a 1.8 % error rate, but the peak at the 615.4 m is located amidst the multiple reflection of NJ #1 and the reflected signal of NJ #2. As depicted in Fig. 5(e), the Rényi Entropy value decreases at the positions of each incident and reflected signals, which means that the TF energy is concentrated at the NJs and terminations. However, at approximately 615.4 m, the Rényi entropy also cannot distinguish the two
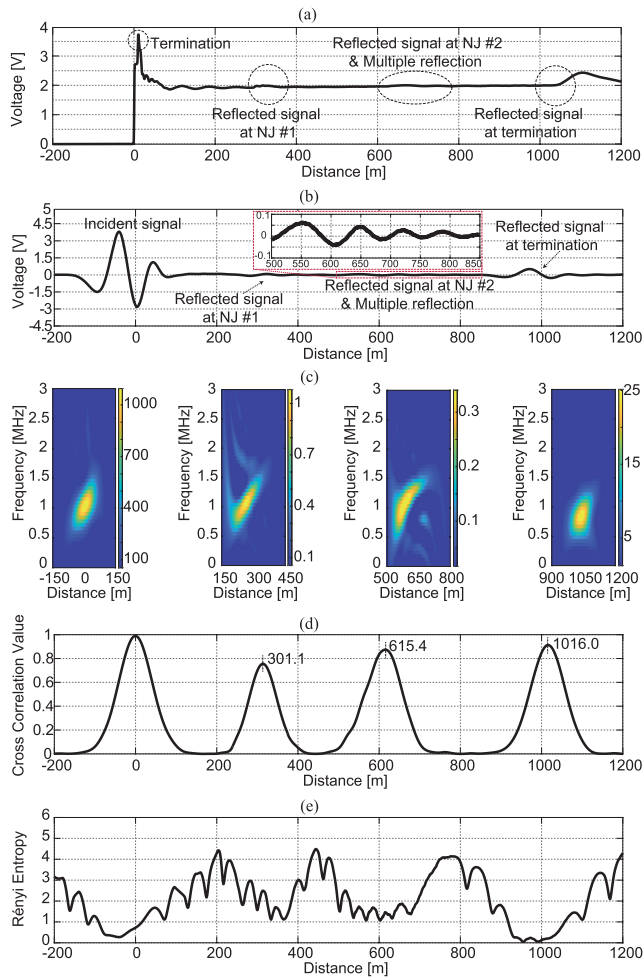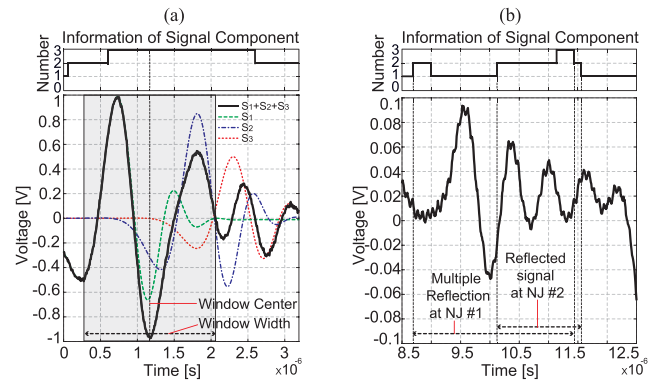
FIGURE 5. (a) TDR data sample in time domain, (b) TFDR data sample in time domain, (c) WVD of the incident signal and reflected signals, (d) TFDR results, and (e) Rényi Entropy.

FIGURE 6. Reflected signals with information of signal component: (a) simulation data and (b) real-world data near NJ #2.

different signals owing to the closeness of the multiple reflection of NJ #1 and the reflected signal of NJ #2.

C. DATASET AND PARAMETER SETTING

Since it is impossible to physically convert the already installed HTS cable system into a large number (e.g. thousands) of combinations, the training of TS-LSTM requires the generation of a dataset via simulation. Therefore, to compare the performance of the proposed TS-LSTM to the conventional TF analysis results, in this work, the reflected signals of the HTS cable system are modeled using MATLAB and Advanced Design System simulations [37]. Three scenarios are used to model the reflected signals: a single signal, two overlapping signals, and three overlapping signals. Fig. 6(a) shows an example of three overlapping signals, S_1, S_2, and S_3. The design parameters of the modeled signals are the same as those of the TFDR incident signal used in this experiment. The magnitude and time center of the three different signals are randomly selected and a total of 450 cases are created. The black straight line in Fig. 6(a) represents one example of the sums of the three overlapping signals. Even in the case of two

overlapping signals, a combination of two different signals produces a total of 450 cases. For the single signal, only the time center is changed, resulting in a total of 225 cases.

For the parameters of the proposed model, the number of hidden units of the TS-LSTM concatenation is set to 650 for short-term TS-LSTM and to 1500 for long-term TS-LSTM. The window size W_L that determines the module length L of the TS-LSTM is set to be equal to the time duration of the incident signal. Training is conducted by classifying the dataset into the two categories of a maximum of two signals in a window (case a), and a maximum of three signals in a window (case b). We do not investigate the case of four or more signals in a single window because the time duration of the incident signal is narrow compared to the resolution of the measuring equipment. Then, 80 % of the dataset is used for training and the remaining 20 % is used for testing.

D. RESULTS IN REAL-WORLD SYSTEM: TS-LSTM

An examination of the data presented in Table 1 shows that the performance of the newly proposed TS-LSTM is improved compared to that of LSTM. In the method column, *a* denotes a case in which up to two signals are present in a window, and *b* denotes a case in which up to three signals are present in a window. For simply distinguishing between a single signal and two signals (case a), better results are obtained when the number of sections, *n*, is equal to 3 (99.27 %). However, it is difficult to determine where $n = 2$ or $n = 3$ is superior for the cases with up to three signals present in a window (case b). $n = 2$ has superior performance for correctly estimating that there are three signals (89.40 %), and $n = 3$ is more accurate for the estimation of the cases where two signals are present (88.62 %). In conclusion, the estimation of the amount of signal energy within the chosen interval (W_L) shows that TS-LSTM further enhances the function of the forget gate even though LSTM can choose which information is relevant for remembering or forgetting. In addition, only the partitioning process itself has the effect of improving LSTM, and the increasing number of sections, n, has no significant effect on improving the TS-LSTM performance.

TABLE 1. Comparative Analysis of Simulation Results.

| Method	Acc. of single signal	Acc. of two signals	Acc. of three signals
LSTMa	100	94.57	N/A
TS-LSTMa (n=2)	100	98.88	N/A
TS-LSTMa (n=3)	100	**99.27**	N/A
LSTMb	100	71.74	63.45
TS-LSTMb (n=2)	100	86.21	**89.40**
TS-LSTMb (n=3)	100	**88.62**	87.95

Fig. 6(a) shows an ideal result where the amount of signal components in a moving window is recorded at the center of the window. Only S_1 is detected at the origin, and the information of the signals component starts with 1, but increases to 2 if S_2 is included in the window, then to 3 by including S_3 near 0.6 μs. Lastly, after 2.5 μs, S_1 disappears from the window, and the number of components returns to 2.

Fig. 6(b) shows the real-world data for the 450-900 m region where NJ #2 is located, as shown in Fig. 4. Using the TS-LSTMb model of Table 1, the signal component information is estimated. At approximately 8.7 μs, an increase in the number of components to 2 means that NJ #1 (296 m) and multiple reflection of NJ #1 (592 m) start entering the same window. From 9 μs, only the multiple reflection is located in the window, but from 10.1 μs, the reflected signal of NJ #2 (627 m) is also seen. Finally, at 11.1 μs, the reflected signal of the termination appears in the window. In conclusion, as shown in Fig. 6(b), the boundaries of the signal component information indicate the sections where the multiple reflection of NJ #1 and reflected signal of NJ #2 are located.

Although conventional methods, TFCC and Rényi Entropy in Fig. 5, cannot distinguish close signal components, TS-LSTM can specify the reflected signal to be analyzed by setting boundary criteria for signal component information. In this work, the main role of the proposed TS-LSTM is to enhance the resolution that distinguishes the reflected signal component of NJ #2 from the multiple reflection of NJ #1. Now, only the reflected signal of NJ #2 can be specified and the phase spectrum of the CT can be extracted from the reflected signal of NJ #2 for monitoring.

E. RESULTS IN REAL-WORLD SYSTEM: CHIRPLET TRANSFORM-BASED MONITORING INDEX

To validate the efficacy of the use of the phase spectrum of CT for the reflected signals distinguished by TS-LSTM, the temperature and pressure data of the AC 154 kV HTS cable systems are measured and compared to the results of the proposed phase spectrum. The pressure and temperature variations are shown in Figs. 7(a) and 7(b), respectively. Since Jeju, South Korea, where the 154 kV HTS cable system is installed, is an island, the supply of liquid nitrogen is unstable and fluctuations are observed in the pressure profile. In addition, the distance between the inlet in the Gumak C/S
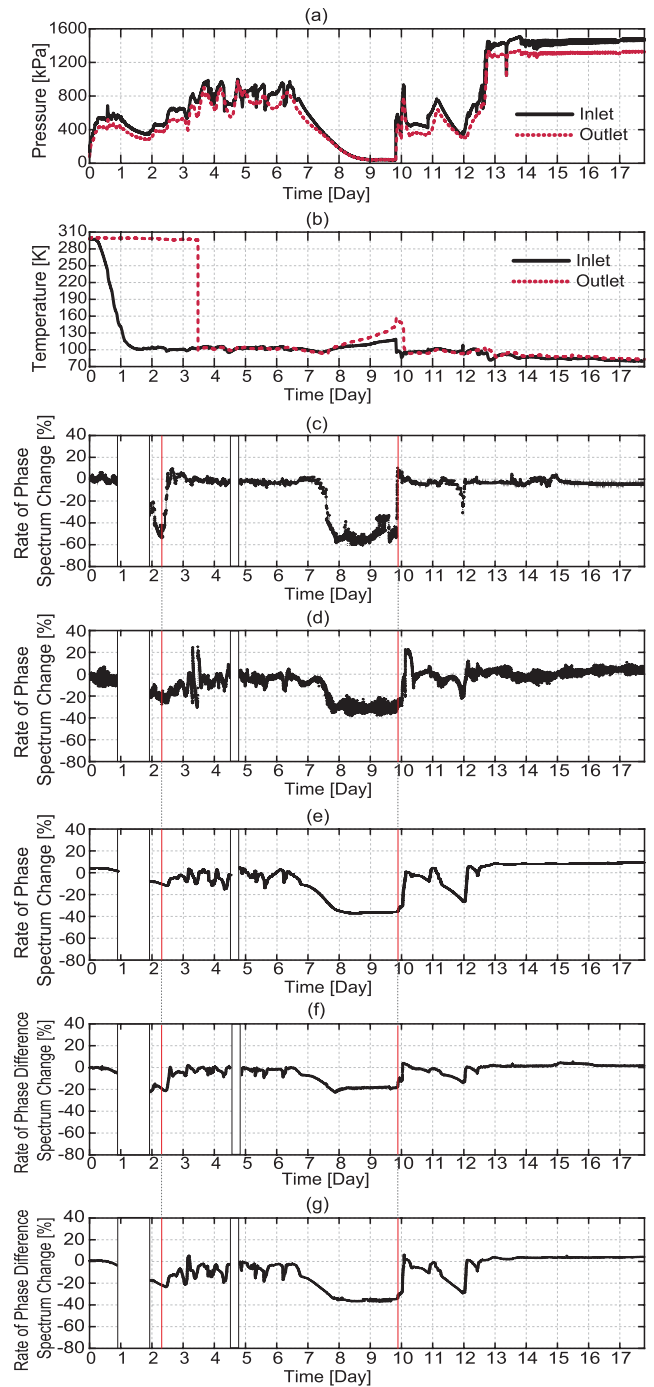
FIGURE 7. Monitoring results of the cooling process in A-phase: (a) pressure profile, (b)temperature profile, (c) phase spectrum of CT at the NJ #1, (d) phase spectrum of CT at the NJ #2, (e) phase spectrum of CT at the termination, (f) phase difference spectrum of WVD at the NJ #1, and (g) phase difference spectrum of WVD at the NJ #2.

and the outlet in the HanLim C/S creates a delay for the both pressure and temperature changes. Therefore, in this section, a comparative analysis of performance is conducted for the dependence of the reaction of the newly proposed phase spectrum of CT and the conventional phase difference spectrum of WVD in previous studie [24], [32] to the fluctuations and

delay. The performance of the two indices is compared for three time periods. In the first time period, a rapid drop in the temperature occurs from day 1 to day 4. In the second time period, pressure fluctuations occur between day 1 and day 6, and finally, a sudden change in both temperature and pressure is observed on day 10.

Figs. 7(c)-(e) show the results of the phase spectrum of CT, and Figs. 7(f)-(g) show the results of the phase difference spectrum of WVD. The areas covered by a white box are the data that are not measured owing to technical errors of the measurement equipment and heavy rain. Because of the limited space, the phase difference spectrum of WVD at the termination is not shown in this paper. However, the results for the two NJs and termination are similar, and the performance of the two indices can be compared and analyzed using the results for two NJs only.

As shown in Fig. 7(b), the temperature of the inlet first drops rapidly on day 1, while the outlet temperature drops on day 4. The results of both indices show a sudden change in the middle of the reaction between the inlet and outlet temperature sensors. The lowest values are found between days 2 and 3 in Figs. 7(c)-(e), where the time positions at which these values are found are in the order of NJ #1 (Fig. 7(c)), NJ #2 (Fig. 7(d)), and termination (Fig. 7(e)). On the other hand, the phase difference spectrum of WVD of NJ #1 (Fig. 7(f)) and NJ #2 (Fig. 7(g)) both have the lowest value at the same time position. The combination of TS-LSTM and phase spectrum of CT detects the time interval between NJ #1 and NJ #2. However, the result of phase difference spectrum of WVD is calculated under the assumption that there are no multiple reflections, so that this result cannot reflect the time interval between two joints.

Second, for the erratic fluctuations of the pressure that occur from day 1 to day 6, both TF-based indices show variations similar to the pressure variation. However, there is more noise in the result of the phase spectrum of CT than in the result of the phase difference spectrum of the WVD. The changes in the temperature and pressure affect the length and the propagation characteristics of the HTS cable system. As the propagation characteristics change, the speed of the incident signal varies. Thus, there is less noise in the index of (12) that responds predominantly to the speed.

Lastly, on day 10, the temperature of the inlet first decreased and then the temperature of the outlet decreased rapidly. As shown in Figs. 7(c)-(e), the index which is calculated from the CT responds to the temperature change in the order of the reflected signal position, i.e. NJ #1, NJ #2, and termination. Conversely, similar to the result for the time period between days 2 and 3, the index calculated from WVD begins to respond to the temperature at the same location.

In conclusion, both the phase spectrum of CT and the phase difference spectrum of WVD respond similarly to the temperature and pressure variations that occur during the cooling process of the 154 kV HTS cable system. On the one hand, the index obtained from CT with TS-LSTM networks has the advantage of reflecting the time difference that occurs with the location of the NJs. On the other hand, the index obtained from WVD has the advantage of monitoring the electrical characteristics of the HTS cable without noise. Therefore, the use of both indices is recommended. If the safe operating ranges of both indices are set during normal operation of the HTS cable system, the two indices can be effectively used to estimate the failure time and fault location of the HTS cable system. In fact, the temperature sensors of the HTS cables are installed in the cryostats of the HTS cables, so that temperature data acquired from the sensors are different from the actual temperatures of the superconducting layer. Both the phase spectrum of the CT and the phase difference spectrum of the WVD are expected to react faster than the temperature sensors because these two indices are affected by the insulation temperature and pressure.

V. CONCLUSION

This paper proposes a monitoring method considering the installation environment and electrical characteristics of HTS cable systems. The main contribution of the proposed monitoring method is that, by using the AC 154 kV 600 MVA HTS cable system connected to a real electric power grid, the phase spectrum derived from CT has shown to be able to monitor the real-time status of wave propagation characteristics during the cooling process. Furthermore, TS-LSTM is introduced to distinguish the multiple reflections and reflected signals with higher resolution than conventional signal information measurement methods.

In future work, controllable parameters of TS-LTSM module such as partition number, length of module, and temporal stride need to be optimized. Therefore, the searching method to find optimal numbers for parameters of TS-LTSM module will be studied. Additionally, a study on the feature extraction other than time-frequency analysis by Wigner-Ville distribution is required. Thus, advanced signal analysis for electrical signals, vibration signals, and audible signals will be studied to develop robust features for the diagnosis of HTS cable systems. Lastly, South Korea is currently preparing to connect AC 22.9 kV tri-axial HTS cable systems near Seoul to the actual electric power grid. Unlike conventional HTS cables, a tri-axial cable is composed of three concentric phases, such that the characteristics of the tri-axial HTS cable are expected to be different. Therefore, a monitoring method optimized for the tri-axial HTS cable will be studied.

The proposed monitoring method using TS-LSTM will improve the utilization of HTS cable systems in urban areas where power consumption is rapidly increasing. In the operation of HTS cable systems, electrical characteristic monitoring will enable maintenance and ensure operational stability.

REFERENCES

[1] C. Rey, *Superconductors in the Power Grid: Materials and Applications*. Cambridge, U.K.: Elsevier, 2015.

[2] J. F. Maguire, F. Schmidt, S. Bratt, T. E. Welsh, J. Yuan, A. Allais, and F. Hamber, "Program update on the development and demonstration of a HTS power cable to operate in the long island power authority transmission grid," in *Proc. IEEE Power Eng. Soc. Gen. Meeting*, Tampa, FL, USA, Jun. 2007, pp. 1–4.

[3] L. Xiao, S. Dai, L. Lin, J. Zhang, W. Guo, D. Zhang, Z. Gao, N. Song, Y. Teng, Z. Zhu, Z. Zhang, G. Zhang, F. Zhang, X. Xu, W. Zhou, Q. Qiu, and H. Li, "Development of the World's first HTS power substation," *IEEE Trans. Appl. Supercond.*, vol. 22, no. 3, Jun. 2012, Art. no. 5000104.

[4] M. Stemmle, F. Merschel, M. Noe, and A. Hobl, "AmpaCity—Advanced superconducting medium voltage system for urban area power supply," in *Proc. IEEE PES T&D Conf. Expo.*, Chicago, IL, USA, Apr. 2014, pp. 1–5.

[5] C. Lee, J. Choi, H. Yang, M. Park, and M. Iwakuma, "Economic evaluation of 23 kV tri-axial HTS cable application to power system," *IEEE Trans. Appl. Supercond.*, vol. 29, no. 5, Aug. 2019, Art. no. 5402507.

[6] X. Peng, J. Li, G. Wang, Y. Wu, L. Li, Z. Li, A. Ahmed Bhatti, C. Zhou, D. M. Hepburn, A. J. Reid, M. D. Judd, and W. H. Siew, "Random forest based optimal feature selection for partial discharge pattern recognition in HV cables," *IEEE Trans. Power Del.*, vol. 34, no. 4, pp. 1715–1724, Aug. 2019.

[7] F.-C. Gu, H.-T. Yau, and H.-C. Chen, "Application of chaos synchronization technique and pattern clustering for diagnosis analysis of partial discharge in power cables," *IEEE Access*, vol. 7, pp. 76185–76193, 2019.

[8] M. Mahdipour, A. Akbari, P. Werle, and H. Borsi, "Partial discharge localization on power cables using on-line transfer function," *IEEE Trans. Power Del.*, vol. 34, no. 4, pp. 1490–1498, Aug. 2019.

[9] M. Shafiq, I. Kiitam, P. Taklaja, L. Kutt, K. Kauhaniemi, and I. Palu, "Identification and location of PD defects in medium voltage underground power cables using high frequency current transformer," *IEEE Access*, vol. 7, pp. 103608–103618, 2019.

[10] X. Hu, W. H. Siew, M. D. Judd, A. J. Reid, and B. Sheng, "Modeling of high-frequency current transformer based partial discharge detection in high-voltage cables," *IEEE Trans. Power Del.*, vol. 34, no. 4, pp. 1549–1556, Aug. 2019.

[11] M. Li, C. Zhou, and W. Zhou, "A revised model for calculating HV cable sheath current under short-circuit fault condition and its application for fault location—Part 1: The revised model," *IEEE Trans. Power Del.*, vol. 34, no. 4, pp. 1674–1683, Aug. 2019.

[12] M. A. Shokry, A. Khamlichi, F. Garnacho, J. M. Malo, and F. Alvarez, "Detection and localization of defects in cable sheath of cross-bonding configuration by sheath currents," *IEEE Trans. Power Del.*, vol. 34, no. 4, pp. 1401–1411, Aug. 2019.

[13] X. Dong, Y. Yang, C. Zhou, and D. M. Hepburn, "Online monitoring and diagnosis of HV cable faults by sheath system currents," *IEEE Trans. Power Del.*, vol. 32, no. 5, pp. 2281–2290, Oct. 2017.

[14] R. Neimanis, R. Eriksson, and R. Papazyan, "Diagnosis of moisture in oil/paper distribution Cables—Part II: Water penetration in cable insulation-experiment and modeling," *IEEE Trans. Power Del.*, vol. 19, no. 1, pp. 15–20, Jan. 2004.

[15] A. Ghaderi, A. Mingotti, F. Lama, L. Peretto, and R. Tinarelli, "Effects of temperature on MV cable joints tan delta measurements," *IEEE Trans. Instrum. Meas.*, vol. 68, no. 10, pp. 3892–3898, Oct. 2019.

[16] C. Gao, L. Wang, J. Mao, S. Hu, B. Zhang, and S. Yang, "Non-intrusive cable fault diagnosis based on inductive directional coupling," *IEEE Trans. Power Del.*, vol. 34, no. 4, pp. 1684–1694, Aug. 2019.

[17] G.-Y. Kwon, C.-K. Lee, G. S. Lee, Y. H. Lee, S. J. Chang, C.-K. Jung, J.-W. Kang, and Y.-J. Shin, "Offline fault localization technique on HVDC submarine cable via time–frequency domain reflectometry," *IEEE Trans. Power Del.*, vol. 32, no. 3, pp. 1626–1635, Jun. 2017.

[18] Y. Huo, G. Prasad, L. Atanackovic, L. Lampe, and V. C. M. Leung, "Cable diagnostics with power line modems for smart grid monitoring," *IEEE Access*, vol. 7, pp. 60206–60220, 2019.

[19] I. M. Karmacharya and R. Gokaraju, "Fault location in ungrounded photovoltaic system using wavelets and ANN," *IEEE Trans. Power Del.*, vol. 33, no. 2, pp. 549–559, Apr. 2018.

[20] M. S. Kemper, C. Philippczyk, R. J. Rayzak, and V. Waschk, "A new method for the detection and quantification of residual volatiles in XLPE electrical cable using large-spot Raman spectroscopy," *IEEE Trans. Power Del.*, vol. 26, no. 1, pp. 3–10, Jan. 2011.

[21] H.-M. Chang, K. N. Ryu, and H. S. Yang, "Cryogenic design of liquid-nitrogen circulation system for long-length HTS cables with altitude variation," *Cryogenics*, vol. 83, pp. 50–56, Apr. 2017.

[22] M. Yanuka, G. C. Topp, S. Zegelin, and W. D. Zebchuk, "Multiple reflection and attenuation of time domain reflectometry pulses: Theoretical considerations for applications to soil and water," *Water Resour. Res.*, vol. 24, no. 7, pp. 939–944, Jul. 1988.

[23] C.-P. Lin, Y. J. Ngui, and C.-H. Lin, "Multiple reflection analysis of TDR signal for complex dielectric spectroscopy," *IEEE Trans. Instrum. Meas.*, vol. 67, no. 11, pp. 2649–2661, Nov. 2018.

[24] G. S. Lee, S. S. Bang, G.-Y. Kwon, Y. H. Lee, S.-H. Sohn, S.-C. Han, and Y.-J. Shin, "Time—Frequency-based condition monitoring of 22.9-kV HTS cable systems: Cooling process and current imbalance," *IEEE Trans. Ind. Electron.*, vol. 66, no. 10, pp. 8116–8125, Oct. 2019.

[25] S. Mann and S. Haykin, "The chirplet transform: Physical considerations," *IEEE Trans. Signal Process.*, vol. 43, no. 11, pp. 2745–2761, Nov. 1995.

[26] Y. Yang, Z. K. Peng, G. Meng, and W. M. Zhang, "Spline-kernelled chirplet transform for the analysis of signals with time-varying frequency and its application," *IEEE Trans. Ind. Electron.*, vol. 59, no. 3, pp. 1612–1621, Mar. 2012.

[27] I. Lee, D. Kim, S. Kang, and S. Lee, "Ensemble deep learning for skeleton-based action recognition using temporal sliding LSTM networks," in *Proc. IEEE Int. Conf. Comput. Vis. (ICCV)*, Venice, Italy, Oct. 2017, pp. 1012–1020.

[28] I. Lee, D. Kim, and S. Lee, "3D human behavior understanding using generalized TS-LSTM networks," *IEEE Trans. Multimedia*, early access, Mar. 5, 2020, doi: 10.1109/TMM.2020.2978637.

[29] J. Wang, Z. Liu, Y. Wu, and J. Yuan, "Mining actionlet ensemble for action recognition with depth cameras," in *Proc. IEEE Conf. Comput. Vis. Pattern Recognit.*, Providence, RI, USA, Jun. 2012, pp. 1290–1297.

[30] Y. Du, Y. Fu, and L. Wang, "Representation learning of temporal dynamics for skeleton-based action recognition," *IEEE Trans. Image Process.*, vol. 25, no. 7, pp. 3010–3022, Jul. 2016.

[31] B. Boashash and P. Black, "An efficient real-time implementation of the Wigner-Ville distribution," *IEEE Trans. Acoust., Speech, Signal Process.*, vol. 35, no. 11, pp. 1611–1618, Nov. 1987.

[32] G. S. Lee, G.-Y. Kwon, S. S. Bang, Y. H. Lee, S.-H. Sohn, K. Park, and Y.-J. Shin, "Monitoring electrical and thermal characteristics of HTS cable systems via time–frequency domain reflectometry," *IEEE Trans. Appl. Supercond.*, vol. 27, no. 4, Jun. 2017, Art. no. 9000605.

[33] G. S. Lee, "Time-frequency based analysis of wave propagation characteristics in cooling process of AC 154 kV HTS cable system," in *Proc. 10th Int. Conf. Insulated Power Cables*, Paris, France, Jun. 2019, pp. 1–5.

[34] A. Rényi, "On measures of entropy and information," in *Proc. 4th Berkeley Symp. Math. Statist. Probab.*, vol. 1, 1961, pp. 547–561.

[35] W. J. Williams, M. L. Brown, and A. O. Hero, "Uncertainty, information, and time-frequency distributions," *Proc. SPIE*, vol. 1566, pp. 144–156, Dec. 1991.

[36] Y.-J. Shin, E. J. Powers, T.-S. Choe, C.-Y. Hong, E.-S. Song, J.-G. Yook, and J. B. Park, "Application of time-frequency domain reflectometry for detection and localization of a fault on a coaxial cable," *IEEE Trans. Instrum. Meas.*, vol. 54, no. 6, pp. 2493–2500, Dec. 2005.

[37] G.-Y. Kwon, S. S. Bang, Y. H. Lee, G. S. Lee, and Y.-J. Shin, "Modeling of high-temperature superconducting cable via time domain reflectometry and general regression neural network," *IEEE Trans. Appl. Supercond.*, vol. 29, no. 5, Aug. 2019, Art. no. 5401605.

GEON SEOK LEE (Member, IEEE) received the B.S. and Ph.D. degrees from the School of Electrical and Electronic Engineering, Yonsei University, Seoul, South Korea, in 2014 and 2020, respectively. His current research interests include condition monitoring, health index, diagnosis of cable, advanced signal processing technique, superconducting cable, and superconducting transformer for the super grid systems. He was a recipient of the IEEE Council on Superconductivity Graduate Study Fellowship in Applied Superconductivity, in 2018, and the Korea Global Ph.D. Fellowship.

SU SIK BANG (Graduate Student Member, IEEE) received the B.S. degree from the School of Electrical and Electronic Engineering, Yonsei University, Seoul, South Korea, in 2015, where he is currently pursuing the M.S. and Ph.D. degrees. His current research interests include advanced signal processing techniques and machine learning in order to monitor conditions of electrical cable systems.

HOMER ALAN MANTOOTH (Fellow, IEEE) received the B.S. and M.S. degrees in electrical engineering from the University of Arkansas (UA), Fayetteville, AR, USA, in 1985 and 1986, respectively, and the Ph.D. degree from the Georgia Institute of Technology, Atlanta, GA, USA, in 1990. He joined Analogy, Beaverton, OR, USA, a Startup Company, where he focused on semiconductor device modeling and research and development of modeling tools and techniques. In 1998, he joined the Department of Electrical Engineering, UA, as a Faculty Member, where he is currently a Distinguished Professor. In 2005, he helped to establish the National Center for Reliable Electric Power Transmission (NCREPT), UA. He was also an Executive Director of NCREPT and two of its Center of Excellence, such as the NSF Industry/University Cooperative Research Center on Grid-Connected Advanced Power Electronic Systems (GRAPES) and the Cybersecurity Center on Secure, Evolvable Energy Delivery Systems (SEEDS) funded by the U.S. Department of Energy. In 2015, he also helped to establish the UA First NSF Engineering Research Center entitled Power Optimization for Electro-Thermal Systems (POETS), focuses on high-power density systems for transportation applications. His current research interests include analog and mixed-signal IC design and CAD, semiconductor device modeling, power electronics, and power electronic packaging. He was as an Immediate Past President of the IEEE Power Electronics Society, from 2019 to 2020. He is a member of the Tau Beta Pi and the Eta Kappa Nu. He is also a Registered Professional Engineer. He holds the 21st Century Research Leadership Chair in Engineering.

YONG-JUNE SHIN (Senior Member, IEEE) received the B.S. degree in electrical engineering from Yonsei University, Seoul, South Korea, in 1996, the M.S. degree in electrical engineering and computer science from the University of Michigan, Ann Arbor, MI, USA, in 1997, and the Ph.D. degree in electrical and computer engineering from The University of Texas, Austin, TX, USA, in 2004. He joined the Department of Electrical Engineering, University of South Carolina, Columbia, as an Assistant Professor, in 2004, and an Associate Professor with tenure, in 2011. He joined the School of Electrical and Electronic Engineering, Yonsei University, in 2012, and a Professor, in 2017, where he is currently an Associate Dean of the Academic Affairs. He is also a Professor with the School of Electrical and Electronic Engineering. His current research interests include application of advanced digital signal processing techniques to a wide variety of important transient and nonlinear problems in smart electric power grid. He was a recipient of the United States National Science Foundation CAREER Award, in 2008, and the Research and Development Recognition Award from Korea Electric Power Company (KEPCO), in 2016.

● ● ●